High-Resolution Microscopic Ghost Imaging for Bioimaging

Xiao-Hui Zhu,[1] Yan-Feng Bai,[1,*] Wei Tan,[1] Li-Yu Zhou,[1] Xian-Wei Huang,[1] Tong-Ji Jiang,[1] Teng Jiang,[1] Su-Qin Nan,[2] and Xi-Quan Fu[1,†]

[1] *College of Computer Science and Electronic Engineering, Hunan University, Changsha 410082, China*
[2] *School of Computer Science, Hunan University of Technology and Business, Changsha 410205, China*

(Received 12 November 2022; revised 29 April 2023; accepted 23 June 2023; published 13 July 2023)

A label-free, low-photodamage, low-cost, and *in vivo* high-resolution microscopic imaging technique has been challenging to develop. Ghost imaging (GI) is a computational imaging protocol with the spatially nonlocal property, which enables low-light imaging. Considering the advantages of GI, we propose a method, called high-resolution microscopic ghost imaging (HRMGI), to achieve high-resolution imaging by simply demagnifying the signal beam. The analytical formulas for resolution and depth of field (DOF) of HRMGI are provided. Experimental results show that the HRMGI system can have 10.5 times higher resolution than the conventional GI, which can exceed the pixel size limit of multipixel detectors, and 58 times greater DOF than the traditional diffraction-limited optical (TDLO) system. To present the performance of HRMGI, blood vessels within an ovarian section are also imaged. The proposed method is expected to facilitate the development of bioimaging techniques and promote the practical application of GI.

DOI: 10.1103/PhysRevApplied.20.014028

I. INTRODUCTION

Microscopic imaging is the primary method to study the structure and function of biological samples. Traditionally, optical microscopy is the main tool for microscopic imaging, but diffraction limits its resolution [1]. Many techniques have been proposed in recent decades to overcome the diffraction limit, such as structured illumination microscopy (SIM) [2], stimulated emission depletion (STED) microscopy [3], photoactivated localization microscopy (PALM) [4], and stochastic reconstruction microscopy (STORM) [5]. However, most methods require fluorescent labeling and long measurement time, which will increase the phototoxicity and photobleaching [6,7]. In addition, modern research-grade microscope equipment is typically complicated and expensive [8,9]. Developing a microscopic imaging technique that is label-free, low-photodamage, low-cost, and capable of *in vivo* high-resolution imaging has been a challenge.

Ghost imaging (GI), as a computational imaging technology, may help provide a solution to the above challenge. During the imaging process, a single-pixel detector, which is referred to as the bucket detector, collects signals that are transmitted or reflected by the imaging target in the signal beam path, and a multipixel detector measures the intensity distribution of the reference beam, which never interacts with the target. Object information can be indirectly obtained by exploiting a cross-correlation between signal beam and reference beam. GI was demonstrated using entangled photon pairs [10]. Further research has shown that the classical thermal light can be used to implement GI [11,12], which gradually led to the study of GI from theoretical research to practical applications. A significant feature of GI is the spatial nonlocal property, i.e., the detection process can be separated from the imaging process of GI. The resolution capability of imaging results comes from the multipixel detector in the reference beam, while the signal beam that interacts with the object provides only intensity fluctuation information. The imaging resolution of GI is determined by the speckle size of the signal beam at the object plane [12–14]. Therefore, reducing the speckle size of the signal beam can improve the resolution. Meanwhile, weakening the signal beam intensity can reduce the phototoxicity and photobleaching. Thus, GI is ideal for bioimaging.

In recent years, many methods to improve the resolution of GI have been developed and can be divided into four categories: sub-Rayleigh imaging, superresolution (SR) algorithms, deep learning, and hyperspectral imaging. Sub-Rayleigh imaging improves the resolution by reducing the width of the point spread function (PSF) of the GI system, including the second- or higher-order correlation [15–17], speckle power spectrum modulation [18,19], and spatial filtering [20,21]. SR algorithms in GI mainly include compressive sensing (CS) [22,23] and deconvolution [24,25]. In particular, CS can obtain SR images at a lower sampling rate than the Nyquist rate. Deep-learning-based GI enables

*yfbai@hnu.edu.cn
†fuxq@hnu.edu.cn

resolution improvements through untrained networks [26, 27]. Hyperspectral GI [28] mainly exploits the difference in spectral dimension between the target and the background to obtain SR images. Though these methods can improve the resolution of GI, they rarely achieve micron-scale resolution in experiments. Moreover, biological tissues have high-transmission characteristics, which result in a weak intensity fluctuation of the transmitted light field and consequently increase the difficulty of obtaining imaging results by GI. Therefore, the real use of GI in biological imaging is uncommon. Padgett *et al.* [29,30] used a quantum entanglement light (QEL) to image wasp wings at low photon numbers in GI. An optimized differential GI protocol was used to image wasp and bug wings using a QEL source in Ref. [31]. Using a conventional inverted microscope, Li *et al.* [32] developed a nanoscopy system based on GI via sparsity constraints. Vinu *et al.* [33] achieved complex-valued object (macroscopic and microscopic) imaging using ghost diffraction and a more sophisticated holographic interference method. However, neither Li *et al.* nor Vinu *et al.* presented imaging results for practical biological tissues.

In this paper, we propose a simple microscopic imaging method called high-resolution microscopic ghost imaging (HRMGI), which can achieve high-resolution imaging by simply reducing the signal beam size using a beam-reduction system. Here, the beam-reduction system reduces the size of the beam without changing its light-field distribution. We provide the analytical formulas for the resolution and depth of field (DOF) in HRMGI, which are verified by the corresponding experimental results. Particularly, imaging results for biological tissues are provided. Theoretical and experimental results show that the imaging resolution of HRMGI can reach the micron scale and exceed the pixel size limit of multipixel detectors, and the HRMGI system can have a much larger DOF than the traditional diffraction-limited optical (TDLO) system. Our results will promote the application of GI in microscopic imaging of biological samples.

II. METHOD

A. Experimental setup and theoretical analysis

The experimental setup of the HRMGI system is depicted in Fig. 1. A diode-pump solid-state laser ($\lambda = 532$ nm) and a rotating ground glass (RGG) are used to produce a pseudothermal light. The filter module includes a $4f$ system and a 150-μm pinhole to improve the quality of the laser beam. The lens L_1 is placed behind the RGG to collect the light scattered by the RGG. The distance between L_1 and RGG is equal to the focal length $f_1 = 50$ mm of L_1. Then, the light beam is blocked by stop 1 of radius w_s at the back focal plane of L_1. Thus, the plane where stop 1 is located can be taken as the original plane of a pseudothermal source with transversal size

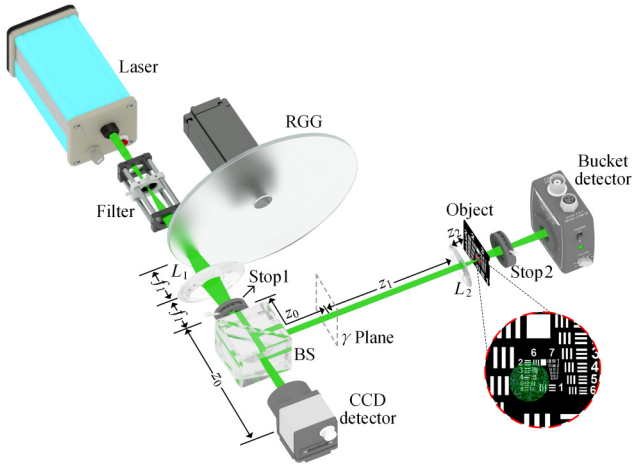

FIG. 1. Experimental schematic of HRMGI. Filter: filter module. It consists of two lenses and a 150-μm pinhole. BS, beam splitter; RGG, rotating ground glass. The RGG and stop 1 are located at the front and rear focal planes of lens L_1, respectively. z_0 is the distance between stop 1 and the CCD and γ plane. As the beam reduction system, lens L_2 demagnifies the signal beam at the γ plane. The enlarged red dashed circle indicates the approximate location of the object to be imaged, and the green circular area indicates the speckle field at the object plane.

$2w_s$. A nonpolarizing beam splitter (BS), which is near stop 1, divides the incident beam into the signal and reference beams. Photons of the signal beam are collected by the bucket detector (Thorlabs PDA100A2) after passing through lens L_2 with focal length f and diameter D, an object, and stop 2. The distance between the object and L_2 is z_2. The beam-reduction system in this experiment is lens L_2. The intensity distribution of the reference beam is detected by the CCD detector (Thorlabs DCC3260C with a pixel size of $\delta_{\text{pixel}} = 5.86$ μm and a total number of pixels of 1936×1216) at distance z_0 from stop 1. To be consistent with the distance in the reference path, we suppose that there is a plane called γ plane in the signal beam path, which has distances z_0 and z_1 to stop 1 and L_2, respectively. The enlarged red dashed circle in Fig. 1 represents the approximate location of the object to be imaged, and the green circular area indicates the speckle field at the object plane. In addition, distances z_1, z_2, and focal length f satisfy the Gaussian thin lens equation when the object plane is not defocused, i.e., $1/z_1 + 1/z_2 = 1/f$.

According to the statistical optics theory of GI, object information can be obtained by measuring the intensity correlation function of the two beam paths [11]

$$\langle G(\boldsymbol{\rho}_r, \boldsymbol{\rho}_s)\rangle = \left| \int \langle E^*(\boldsymbol{\rho}_1) E(\boldsymbol{\rho}'_2)\rangle \times h_r(\boldsymbol{\rho}_1, \boldsymbol{\rho}_r) h_s^*(\boldsymbol{\rho}'_2, \boldsymbol{\rho}_s) d^2\boldsymbol{\rho}_1 d^2\boldsymbol{\rho}'_2 \right|^2, \quad (1)$$

where $\boldsymbol{\rho}_i$ (i = 1, 2) is the plane coordinates of the light source, and $\langle E^*(\boldsymbol{\rho}_1)E(\boldsymbol{\rho}_2)\rangle$ is the first-order correlation function of the source. $\boldsymbol{\rho}_r$ and $\boldsymbol{\rho}_s$ are the plane coordinates at the CCD detector and object, respectively. $h_r(\boldsymbol{\rho}_1, \boldsymbol{\rho}_r)$ and $h_s(\boldsymbol{\rho}_2, \boldsymbol{\rho}_s)$ are impulse response functions of the reference and signal beam paths, respectively. We suppose that the source is fully incoherent, and the $1/e^2$ diameter of the source is $2w_s$ [13].

Considering the imaging setup in Fig. 1, $h_r(\boldsymbol{\rho}_1, \boldsymbol{\rho}_r)$ is the kernel of the Fresnel diffraction integral [11,34] and $h_s(\boldsymbol{\rho}_2, \boldsymbol{\rho}_s)$ is

$$h_s(\boldsymbol{\rho}_2, \boldsymbol{\rho}_s) \propto \exp\left[\frac{j\pi}{\lambda z}\left(1-\frac{1/z}{b}\right)\boldsymbol{\rho}_2{}^2\right] \times \exp\left[\frac{j\pi}{\lambda z_2}\left(1-\frac{1/z_2}{b}\right)\boldsymbol{\rho}_s{}^2\right] \times \exp\left(-\frac{j2\pi\boldsymbol{\rho}_2\boldsymbol{\rho}_s}{\lambda z z_2 b}\right) t(\boldsymbol{\rho}_s), \quad (2)$$

where $z = z_0 + z_1$ and $b = 1/z + 1/z_2 - 1/f$. $t(\boldsymbol{\rho}_s)$ is the transmission function of the object. By substituting $h_r(\boldsymbol{\rho}_1, \boldsymbol{\rho}_r)$ and $h_s(\boldsymbol{\rho}_2, \boldsymbol{\rho}_s)$ into Eq. (1) and using the related derivation process in Ref. [13], the ghost image is given by

$$G(\boldsymbol{\rho}_r) \propto \int d^2\boldsymbol{\rho}_s \left|t(\boldsymbol{\rho}_s)\right|^2 h(\boldsymbol{\rho}_s, \boldsymbol{\rho}_r) = \int d^2\boldsymbol{\rho}_s \left|t(\boldsymbol{\rho}_s)\right|^2 \exp\left[-\frac{\left(\boldsymbol{\rho}_s - M(dz)\boldsymbol{\rho}_r\right)^2}{\Delta^2(dz)}\right], \quad (3)$$

where $h(\boldsymbol{\rho}_s, \boldsymbol{\rho}_r)$ indicates the PSF of the HRMGI system. $dz = z_2 - z_1 f/(z_1 - f)$ is the defocusing length of the object plane, and $M(dz) = dz(f - z_0 - z_1)/(z_0 f) + f/(f - z_1)$ is the magnification of L_2. When the defocusing length is 0, i.e., $dz = 0$, the magnification of L_2 is $M_0 = M(0) = f/(f - z_1)$. Here, $|M_0|$ is typically less than 1, since the size of the signal beam must be reduced. The $1/e$ radius of $h(\boldsymbol{\rho}_s, \boldsymbol{\rho}_r)$ is denoted by $\Delta(dz)$ and has

$$\Delta^2(dz) = \frac{\alpha_1 + \alpha_2}{(\pi z_0 w_s f)^2}\left\{dz + \frac{z_1 f}{z_1 - f} - \frac{f\left[\alpha_1(z_0 + z_1)/(-f + z_0 + z_1) - \alpha_2 z_1/(f - z_1)\right]}{\alpha_1 + \alpha_2}\right\}^2 + \frac{(z_0 w_s f\lambda)^2}{4(\alpha_1 + \alpha_2)}, \quad (4)$$

where $\alpha_1 = z_0{}^2(-f + z_0 + z_1)^2\lambda^2$ and $\alpha_2 = \pi^2(f - z_1)^2 w_s{}^4/4$. Obviously, α_1 is much smaller than α_2. Thus, Eq. (4) can be simplified as

$$\Delta^2(dz) = \frac{\lambda^2}{\pi^2\delta x^2}dz^2 + \frac{\delta x^2}{4}, \quad (5)$$

with

$$\delta x = \delta x_0 |M_0| = \frac{2\lambda z_0}{\pi w_s}\left|\frac{f}{f - z_1}\right|, \quad (6)$$

δx_0 and δx are the speckle sizes ($1/e$ diameter) at the γ plane and object plane, respectively. The resolution of the system can be defined as $1/e$ full width of $h(\boldsymbol{\rho}_s, \boldsymbol{\rho}_r)$, i.e.,

$$\mathrm{Res}(dz) = 2\sqrt{\frac{\lambda^2}{\pi^2\delta x^2}dz^2 + \frac{\delta x^2}{4}}. \quad (7)$$

Equation (7) shows that the resolution of the HRMGI system reaches its minimum value δx when $dz = 0$. This result is consistent with the principle of GI [12–14]. The resolution of some optical systems is limited by diffraction and the pixel size of the detector. δx may be smaller than the pixel size δ_{pixel} of the CCD if one reduces the size of the signal beam in HRMGI. Therefore, the resolution of the HRMGI system can exceed the limit of the CCD pixel size. The radius of the Airy spot at the object plane is determined by the wavelength and numerical aperture (NA) of L_2, i.e., $0.61\lambda/\mathrm{NA}$ [here NA = $D/(2z_2)$] [35]. Although δx can theoretically be smaller than $0.61\lambda/\mathrm{NA}$, it has not been experimentally realized. In addition to the resolution, DOF is useful for imaging systems. Defocusing at the object plane, which is difficult to avoid in practical imaging applications, can reduce the quality of the reconstructed images. Therefore, it is worthwhile to determine the defocusing range, i.e., DOF, within which the imaging results can be resolved. Our group has found that if the center-to-center separation ds of a double-slit is twice the slit width δR, then the double-slit is just distinguishable when the speckle size at the object plane is equal to $2\delta R$ [36]. One of the objects that we image is the triple slit of the UASF resolution chart, whose center-to-center separation is twice its slit width. Thus, we can use a similar criterion to that in Ref. [37] to evaluate the DOF in the HRMGI system. The DOF can be defined as the range of the defocusing length when the resolution $\mathrm{Res}(dz)$ is less than $2\delta R$, i.e., $\mathrm{Res}(dz) \le 2\delta R$. Hence, we obtain

$$z_{\mathrm{DOF}} = 2\sqrt{\left(\delta R^2 - \frac{\delta x^2}{4}\right)\frac{\pi^2\delta x^2}{\lambda^2}}, \quad (8)$$

where z_{DOF} is the DOF of the HRMGI system. Equation (8) can also be expressed in terms of M_0 as follows:

$$z_{\mathrm{DOF}} = 2\sqrt{\frac{-\pi^2\delta x_0{}^4}{4\lambda^2}\left[\left(M_0{}^2 - \frac{2\delta R^2}{\delta x_0{}^2}\right)^2 - \frac{4\delta R^4}{\delta x_0{}^4}\right]}. \quad (9)$$

According to Eq. (9), the DOF can take the maximum value $\pi\delta x^2/\lambda$ when $M_0 = \sqrt{2}\delta R/\delta x_0$. This maximum value is exactly the Rayleigh length of the laser beam with waist spot radius δx. Although Eqs. (8) and (9) are derived based on the assumption that the object is a double slit or triple slit with $ds = 2\delta R$, it is still useful for assessing the DOF of HRMGI systems.

B. Assessment of the image quality

To quantitatively analyze the image quality and calculate the DOF in experiments, we generalize the definition of the R value in Refs. [36,37] and estimate the resolution of the HRMGI system using a genetic algorithm.

In Fig. 2(a), a rectangular box is used to select an area of the reconstructed image that completely contains the object information. This region is vertically integrated and normalized to produce an experimental data curve, i.e., the curve with only circle markers in Fig. 2(b). In Fig. 2(b), P_1, P_3, and P_5 represent the peak values, and P_2 and P_4 represent the valley values of the experimental data. Note that P_1, P_3, and P_5 are not equal in our experiment, nor are P_2 and P_4. Therefore, R is now defined as

$$R = \max\left(\frac{P_2}{\min(P_1, P_3)}, \frac{P_4}{\min(P_3, P_5)}\right), \quad (10)$$

where max and min are the maximum and minimum operators, respectively. According to the Rayleigh criterion [38], two rectangular apertures are considered exactly distinguishable when R is 0.81, i.e., the critical value. A smaller R indicates that it is easier to distinguish the reconstructed image.

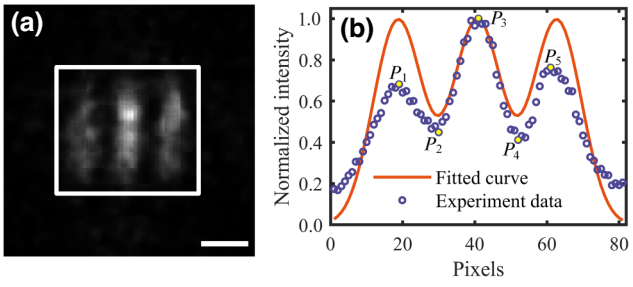

FIG. 2. Method to calculate the R value and estimate the resolution of the reconstructed image. (a) The white rectangular box selects the part of the image that contains information about the object. (b) The curve marked with only circles indicates normalized experimental data. The peak values of the experimental data are represented by P_1, P_3, and P_5, and the valley values are represented by P_2 and P_4. The solid line represents the curve fitted using a Gaussian PSF. Scale bar: 10 μm.

The experimental data curve is fitted by convolution of the standard image of the object with a Gaussian PSF [39]. The Gaussian PSF can be expressed as

$$g(x,y) = c_0 \exp\left[-\frac{(x-c_1)^2 + (y-c_2)^2}{c_3{}^2}\right], \quad (11)$$

where c_0, c_1, c_2, c_3 represent the fitting parameters. A genetic algorithm is used to determine the optimal fitting parameters, and the resolution of the HRMGI system is estimated as the $1/e$ full width of the Gaussian PSF, i.e., $2c_3\delta_{\mathrm{pixel}}|M(dz)|$.

III. RESULTS AND DISCUSSION

Here, we experimentally analyze the resolution and DOF and verify the microimaging capability of the HRMGI system. Throughout the experiment, the values of $w_s = 0.45$ mm and $z_0 = 62$ mm remain unchanged. According to Eq. (6), the speckle size at the CCD plane and γ plane is $\delta x_0 = 46.66$ μm. The values of z_1 and z_2 are not fixed, and the magnification of L_2 depends on them and the focal length f . The number of measurements per reconstructed result is 10 000, and the differential GI algorithm is used [40].

A. Assessing the resolving power of the HRMGI system

We first assess the resolving power of the HRMGI system by imaging micron-scale objects. The focal length f and diameter D of lens L_2 are both 4.5 mm. We select four triple-slits of the resolution chart as imaging objects. They are group 7 element 2 (G7E2), group 7 element 1 (G7E1), group 6 element 6 (G6E6), and group 6 element 5 (G6E5) with slit widths of 3.48, 3.91, 4.38, and 4.92 μm, respectively. The reconstructed images of four triple slits with a dimension of 100 × 100 pixels are shown in Figs. 3(a)–3(c) when dz = 0, and the magnification M_0 of L_2 is −1/10 [Fig. 3(a)], −1/15 [Fig. 3(b)], and −1/20 [Fig. 3(c)]. Figures 3(d) and 3(e) show the R values of the reconstructed images and resolutions of the HRMGI system at different $|M_0|$ values. The experimental values of R and resolution in Figs. 3(d) and 3(e) are the average values acquired by repeating the experiment 4 times. In each experiment, the experimental resolutions at different $|M_0|$ are obtained by averaging the estimated resolution values of the reconstructed images of G6E6 and G6E5. Additionally, ideal reconstructed images generated by convolution between the standard image of the object and the PSF of the HRMGI system are required to calculate the theoretical results.

In Figs. 3(a)–3(c), the portion of the image that contains information about the object is larger when $|M_0|$

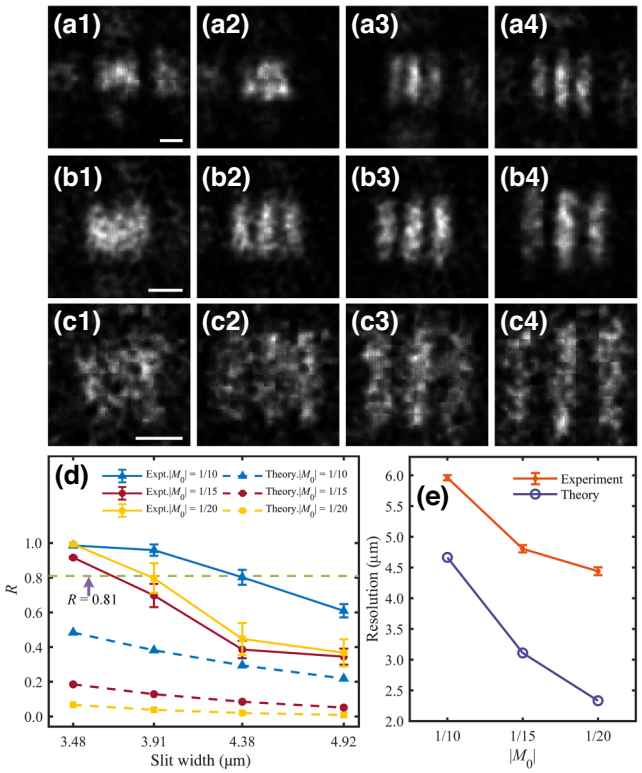

FIG. 3. Experimental results of triple slits in the resolution chart when $dz = 0$. (a) $|M_0| = 1/10$, (b) $|M_0| = 1/15$, (c) $|M_0| = 1/20$. (a1), (b1), (c1) Group 7 element 2. (a2), (b2), (c2) Group 7 element 1. (a3), (b3), (c3) Group 6 element 6. (a4), (b4), (c4) Group 6 element 5. (d) R values of the reconstructed images. (e) Resolutions of different $|M_0|$. Error bars in (d) and (e) represent the standard deviation. Scale bar: 10 μm.

decreases because δx also decreases. Figure 3(d) indicates whether the reconstructed image can be distinguished by the R value. When $|M_0| = 1/10$, the experimental R value for G7E2 and G7E1 is greater than the critical value of 0.81, close to 0.81 for G6E6, and less than 0.81 for G6E5. In other words, G7E2 and G7E1 are indistinguishable, G6E6 is barely distinguishable, and G6E5 is completely distinguishable. Similarly, when $|M_0| = 1/15$, G7E2 is indistinguishable, whereas G7E1, G6E6, and G6E5 are distinguishable, and when $|M_0| = 1/20$, only G6E6 and G6E5 can be distinguished. Therefore, the HRMGI system with the demonstrated setup can resolve G7E1, G6E6, and G6E5, whose slit widths are smaller than the pixel size of the CCD detector ($\delta_{\text{pixel}} = 5.86$ μm). The experimental resolutions in Fig. 3(e) are 5.96, 4.81, and 4.44 μm when $|M_0| = 1/10$, 1/15, and 1/20, respectively, and the latter two are less than 5.86 μm. This result is evidently much better than the resolution (46.66 μm) when the size of the signal beam is not reduced.

However, all theoretical R values in Fig. 3(d) are less than 0.81, i.e., the corresponding triple slits are theoretically distinguishable. The experimental R value does not always decrease when $|M_0|$ decreases. For example, the corresponding R value at $|M_0| = 1/20$ is greater than that at $|M_0| = 1/15$. Meanwhile, the resolution improves when $|M_0|$ decreases despite an increase in difference between experimental and theoretical values, as shown in Fig. 3(e). Thus, the system is not necessarily able to resolve smaller objects by continuously demagnifying the signal beam in experiments. This result may be due to two factors: noise and aberration. The noise includes correlation noise, stray light noise and detector noise. Correlation noise is caused by the incomplete independence between speckle fields, which reduces the SNR of the reconstructed images [41]. Stray-light noise refers to stray light around the object, which also reduces the SNR of the image, and a smaller object is more adversely affected by stray-light noise [42]. Therefore, stop 2 in Fig. 1 is imperative to block stray light. The detector noise can significantly affect the imaging quality under low light or photon-counting conditions. Meanwhile, aberration is caused by the nonideal beam-reduction system (in this case, the lens L_2). A single lens cannot correct all aberrations, and the resulting wave-front aberrations can negatively affect the spot focusing. The finite aperture of the lens also limits the high-frequency component of the beam. Moreover, the reduction of the size of the signal beam reduces δx and makes the photon-number distribution of the optical field at the object plane more concentrated, which even approaches the diffraction limit. Therefore, the wave nature of the beam is more pronounced at the object plane than at the CCD plane.

In summary, we can image micron-scale objects using a simple and low-cost device based on HRMGI. The HRMGI system can resolve the G7E1 of the resolution chart, which has a slit width of 3.91 μm. The resolution of the system improves 10.5-fold (46.66/4.44) compared to the case without demagnifying the signal beam, and it can exceed the CCD pixel-size limit. The experiment results strongly demonstrate the capability of the HRMGI method for imaging at the microscopic level.

B. Calculating the depth of field

The DOF of the HRMGI system is examined in this section. The system parameters are identical to those in Sec. III A, and $|M_0| = 1/15$. The object is G6E6 of the resolution chart. Figure 4 shows the reconstructed images with a dimension of 100 × 100 pixels at different defocusing lengths dz, where dz increases from −90 to 120 μm in increments of 30 μm (we reconstruct the image with dz changing every 10 μm and Fig. 4 demonstrates only part of the results). The reconstructed images gradually become blurry as $|dz|$ increases.

Figure 5(a) shows the curve of the R value as a function of dz to calculate the DOF. Both theoretical and experimental R values gradually increase when $|dz|$ increases. For dz of −70 and 70 μm, the theoretical and experimental

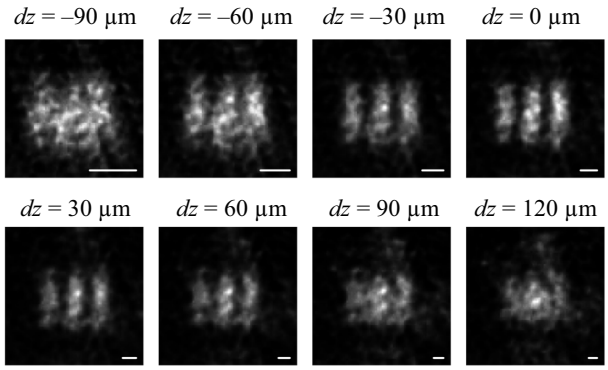

FIG. 4. Experimental results for G6E6 at different defocusing lengths dz when $|M_0| = 1/15$. The value of dz varies from −90 to 120 μm in increments of 30 μm. The number of pixels per image is 100 × 100. Scale bar: 5 μm.

R values are approximately 0.81. Accordingly, the experimental DOF value is approximately 140 μm, i.e., the range between the two red dashed lines in Fig. 5(a). The relative error between this experimental value and the theoretical value of 150.4 μm calculated by Eq. (8) is approximately 6.9%. Meanwhile, the two gray dashed lines in Fig. 5(a) indicate the DOF of L_2 as $\lambda/\mathrm{NA}^2 \approx 2.42$ μm [35,43]. The DOF of the HRMGI system is approximately 58 times that of the TDLO system with a lens. Figure 5(b) also shows that the theoretical and experimental resolutions roughly match each other when dz is in the DOF range.

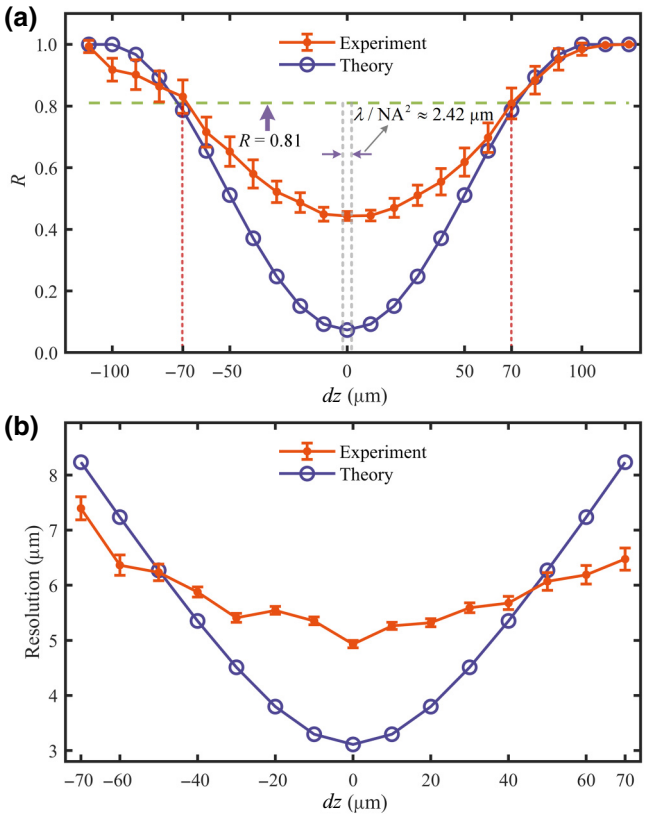

FIG. 5. R values and resolutions of G6E6 with different defocusing lengths dz when $|M_0| = 1/15$. (a) Theoretical and experimental R values. (b) Theoretical and experimental resolutions in the DOF range. Error bars in (a),(b) represent the standard deviation.

The DOF in a TDLO system is determined by reducing the light intensity along the optical axis to 80% of the intensity at the center of the object plane [35,43]. However, according to Eq. (8), the DOF of HRMGI systems not only depends on the speckle size δx at the object plane, but also on the minimum details of the object (here, it refers to the slit width δR of the triple slit). The maximum value of DOF of the HRMGI system, i.e., $\pi\delta x^2/\lambda$, is independent of δR and proportional to the negative power of the wavelength λ, while the DOF of TDLO systems is proportional to the power of λ. Therefore, for a given object to be imaged, although the DOF of the HRMGI system tends to 0 when δx tends to 0 or $2\delta R$, it is still larger than that of the TDLO system in the vast majority of cases when $\delta x \in (0, 2\delta R)$.

In summary, the HRMGI system can achieve a much greater DOF than the TDLO system, which will greatly reduce operational difficulties during experiments and make it easier to obtain better imaging results.

C. Imaging of biological samples

The high-resolution capability and large DOF of the HRMGI system and the controllable intensity of the signal beam, which interacts with the object, make it very suitable for biological imaging. Thus, we demonstrate the bioimaging capability of the HRMGI system in this section using biological cell samples. $|M_0|$ is selected as 1/5 and 1/8, and $f = 10$ mm. The object is the medullary region of the ovary section. Figures 6(a)–6(c) show the imaging results of the common light microscope (magnification 100×) and the HRMGI system at $|M_0| = 1/5$ and 1/8. The image size in Figs. 6(a) and 6(b) is 180 × 180 pixels, and the size of Fig. 6(c) is set to 288 × 288 to have the same field of view (FOV) as that in Fig. 6(b). Accordingly, the experimental results of the DOF of the HRMGI system are approximately 450 and 350 μm when $|M_0| = 1/5$ and 1/8, respectively. The brighter areas marked with pentagrams in Fig. 6(a) are blood vessels, which are approximately a few to a dozen microns in size. As shown in Figs. 6(b) and 6(c), the HRMGI system can relatively clearly and completely obtain an image of these areas. Figure 6(c) shows smaller details of the blood vessels and a relatively higher noise level than Fig. 6(b). This result is consistent with the analysis in Sec. III A. In addition, the FOV of the imaging result decreases when $|M_0|$ decreases. Therefore, the edges of the image in Fig. 6(c) are less clear compared to Fig. 6(b) under the same FOV.

Biological samples are generally highly transparent, which results in a weak fluctuation of the signal that carries the object information. Thus, noise is more likely to affect

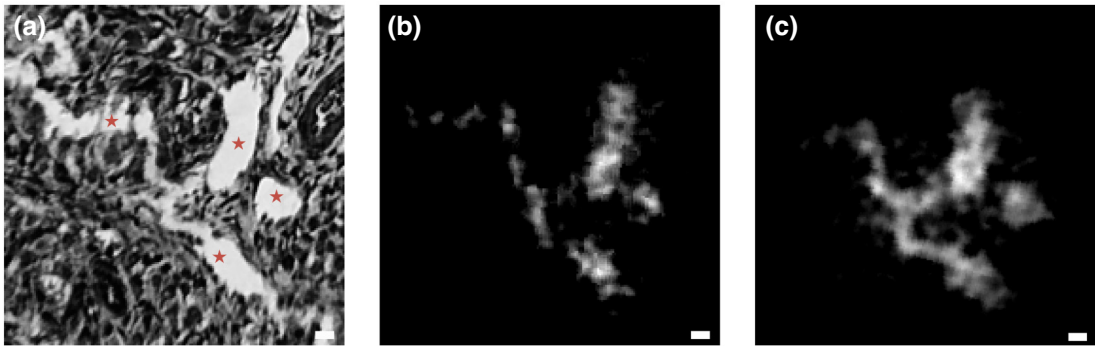

FIG. 6. Imaging results of an ovary section. (a) Result of a common light microscope with a magnification of 100×. Pentagrams indicate blood vessels in the medullary region. (b) Experiment result of the HRMGI system with $|M_0| = 1/5$. (c) Experiment result of the HRMGI system with $|M_0| = 1/8$. Scale bar: 10 μm.

the imaging of biological samples in HRMGI. Correlation noise can be reduced by using quantum entanglement light sources or light sources modulated in orthogonal patterns (e.g., those modulated by Hadamard matrices). The photon-counting method can be used instead of the bucket detector to improve the image quality under low-light illumination conditions. The reason is that the photon counting method increases the dynamic range of the detection system and consequently improves the SNR of the reconstructed images [44]. Combining other GI algorithms or superresolution algorithms can also improve the resolution and SNR of the reconstructed images.

As mentioned in Sec. II A, DOF is also important for practical imaging. Conventional microscopes are limited in their three-dimensional imaging capabilities by a small DOF [45], whereas the HRMGI shows significant advantages in this regard. The NA of the objective of the microscope in the experiment is 0.25, so the DOF is approximately 8.5 μm. The DOF of the HRMGI system at $|M_0| = 1/5$ and 1/8 is 53 times and 41 times larger than this value, respectively. Thus, HRMGI has practical application value in microscopic imaging.

In summary, the imaging results in Figs. 6(b) and 6(c) enable further applications of HRMGI in biological imaging. HRMGI does not require staining biological samples, so it promises label-free, long-term *in vivo* imaging. The main drawback of the current HRMGI prototype is that it is highly affected by noise. As previously discussed in this section, the image quality of HRMGI can be further improved from the perspective of light sources, signal detection, and algorithms. In addition, given the great differences in the morphology and size of biological tissues, how HRMGI achieves multiscale imaging is worthy of further study.

IV. CONCLUSION

In conclusion, we propose a method called high-resolution microscopic ghost imaging to achieve high-resolution imaging by only reducing the signal beam size in GI. The analytical expression of the resolution and depth of field are derived. Experimentally, the resolution of the HRMGI system could reach 4.44 μm, and the resolution of the system is improved by up to 10.5 times when compared with the conventional GI and can exceeded the pixel-size limit of the multipixel detector. The DOF of the HRMGI system is approximately 58 times that of the traditional diffraction-limited optical system, and it can be even larger. In addition, HRMGI shows potential and advantages in imaging biological samples, and it is expected to facilitate the development of bioimaging techniques using simple and low-cost equipment.

It is possible to improve the resolution of the actual HRMGI system by reducing the impact of noise. A better beam-reduction system can reduce aberrations, which is also necessary for HRMGI. Furthermore, if the magnification $|M_0|$ is sufficiently small, the speckle size δx at the object plane can theoretically be smaller than the Airy spot of the demagnified signal beam. Consequently, the resolution of the HRMGI system may exceed the diffraction limit at this time. However this will be a very challenging problem because it is currently difficult to experimentally verify this idea due to noise effects and technical limitations.

ACKNOWLEDGMENTS

This work is supported by the National Natural Science Foundation of China (Grants No. 61871431, No. 61971184, No. 62001162, and No. 62101187), the Hunan Provincial Natural Science Foundation of China (2022JJ40091), and the Fundamental Research Funds for the Central Universities (531118010757).

[1] B. R. Masters, *Superresolution Optical Microscopy: The Quest for Enhanced Resolution and Contrast* (Springer, Cham, Switzerland, 2020), Vol. 227.

[2] M. G. Gustafsson, Surpassing the lateral resolution limit by a factor of two using structured illumination microscopy, J. Microsc. **198**, 82 (2000).

[3] S. W. Hell and J. Wichmann, Breaking the diffraction resolution limit by stimulated emission: Stimulated-emission-depletion fluorescence microscopy, Opt. Lett. **19**, 780 (1994).

[4] E. Betzig, G. H. Patterson, R. Sougrat, O. W. Lindwasser, S. Olenych, J. S. Bonifacino, M. W. Davidson, J. Lippincott-Schwartz, and H. F. Hess, Imaging intracellular fluorescent proteins at nanometer resolution, Science **313**, 1642 (2006).

[5] M. J. Rust, M. Bates, and X. Zhuang, Sub-diffraction-limit imaging by stochastic optical reconstruction microscopy (storm), Nat. Methods **3**, 793 (2006).

[6] Editorial, Artifacts of light, Nat. Methods **10**, 1135 (2013),.

[7] S. Waldchen, J. Lehmann, T. Klein, S. van de Linde, and M. Sauer, Light-induced cell damage in live-cell super-resolution microscopy, Sci. Rep. **5**, 15348 (2015).

[8] A. Bullen, Microscopic imaging techniques for drug discovery, Nat. Rev. Drug Discov. **7**, 54 (2008).

[9] B. Diederich, R. Lachmann, S. Carlstedt, B. Marsikova, H. Wang, X. Uwurukundo, A. S. Mosig, and R. Heintzmann, A versatile and customizable low-cost 3D-printed open standard for microscopic imaging, Nat. Commun. **11**, 5979 (2020).

[10] T. B. Pittman, Y. H. Shih, D. V. Strekalov, and A. V. Sergienko, Optical imaging by means of two-photon quantum entanglement, Phys. Rev. A **52**, R3429 (1995).

[11] J. Cheng and S. S. Han, Incoherent Coincidence Imaging and its Applicability in X-Ray Diffraction, Phys. Rev. Lett. **92**, 093903 (2004).

[12] F. Ferri, D. Magatti, A. Gatti, M. Bache, E. Brambilla, and L. A. Lugiato, High-Resolution Ghost Image and Ghost Diffraction Experiments with Thermal Light, Phys. Rev. Lett. **94**, 183602 (2005).

[13] Y. Gao, Y. F. Bai, and X. Q. Fu, Point-spread function in ghost imaging system with thermal light, Opt. Express **24**, 25856 (2016).

[14] W. L. Gong and S. S. Han, High-resolution far-field ghost imaging via sparsity constraint, Sci. Rep. **5**, 9280 (2015).

[15] P. L. Zhang, W. L. Gong, X. Shen, D. J. Huang, and S. S. Han, Improving resolution by the second-order correlation of light fields, Opt. Lett. **34**, 1222 (2009).

[16] J. E. Oh, Y. W. Cho, G. Scarcelli, and Y. H. Kim, Sub-Rayleigh imaging via speckle illumination, Opt. Lett. **38**, 682 (2013).

[17] F. Li, C. Altuzarra, T. Li, M. O. Scully, and G. S. Agarwal, Beyond sub-Rayleigh imaging via high order correlation of speckle illumination, J. Opt. **21**, 115604 (2019).

[18] S. Z. Zhang, W. Wang, R. Yu, and X. X. Yang, High-order correlation of non-Rayleigh speckle fields and its application in super-resolution imaging, Laser Phys. **26**, 055007 (2016).

[19] E. F. Zhang, H. Z. Lin, W. T. Liu, Q. Li, and P. X. Chen, Sub-Rayleigh-diffraction imaging via modulating classical light, Opt. Express **23**, 33506 (2015).

[20] X. H. Chen, F. H. Kong, Q. Fu, S. Y. Meng, and L. A. Wu, Sub-Rayleigh resolution ghost imaging by spatial low-pass filtering, Opt. Lett. **42**, 5290 (2017).

[21] J. Sprigg, T. Peng, and Y. H. Shih, Super-resolution imaging using the spatial-frequency filtered intensity fluctuation correlation, Sci. Rep. **6**, 1 (2016).

[22] B. Lochocki, K. Abrashitova, J. F. de Boer, and L. V. Amitonova, Ultimate resolution limits of speckle-based compressive imaging, Opt. Express **29**, 3943 (2021).

[23] M. F. Duarte, M. A. Davenport, D. Takhar, J. N. Laska, T. Sun, K. F. Kelly, and R. G. Baraniuk, Single-pixel imaging via compressive sampling, IEEE Signal Process. Mag. **25**, 83 (2008).

[24] Z. P. Chen, J. H. Shi, Y. Li, Q. Li, and G. H. Zeng, Super-resolution thermal ghost imaging based on deconvolution, Eur. Phys. J. Appl. Phys. **67**, 10501 (2014).

[25] Z. S. Tong, Z. T. Liu, C. Y. Hu, J. Wang, and S. S. Han, Preconditioned deconvolution method for high-resolution ghost imaging, Photon. Res. **9**, 1069 (2021).

[26] S. P. Liu, X. F. Meng, Y. K. Yin, H. Z. Wu, and W. J. Jiang, Computational ghost imaging based on an untrained neural network, Opt. Lasers Eng. **147**, 106744 (2021).

[27] F. Wang, C. L. Wang, M. L. Chen, W. L. Gong, Y. Zhang, S. S. Han, and G. H. Situ, Far-field super-resolution ghost imaging with a deep neural network constraint, Light: Sci. Appl. **11**, 1 (2022).

[28] Z. S. Tong, Z. T. Liu, J. Wang, X. Shen, and S. S. Han, Breaking Rayleigh's criterion via discernibility in high-dimensional light-field space with snapshot ghost imaging, (2020), arXiv preprint ArXiv:2004.00135.

[29] R. S. Aspden, N. R. Gemmell, P. A. Morris, D. S. Tasca, L. Mertens, M. G. Tanner, R. A. Kirkwood, A. Ruggeri, A. Tosi, R. W. Boyd, G. S. Buller, R. H. Hadfield, and M. J. Padgett, Photon-sparse microscopy: Visible light imaging using infrared illumination, Optica **2**, 1049 (2015).

[30] P. A. Morris, R. S. Aspden, J. E. Bell, R. W. Boyd, and M. J. Padgett, Imaging with a small number of photons, Nat. Commun. **6**, 5913 (2015).

[31] E. Losero, L. Ruo-Berchera, A. Meda, A. Avella, O. Sambataro, and M. Genovese, Quantum differential ghost microscopy, Phys. Rev. A **100**, 063818 (2019).

[32] W. W. Li, Z. S. Tong, K. Xiao, Z. T. Liu, Q. Gao, J. Sun, S. P. Liu, S. S. Han, and Z. Y. Wang, Single-frame wide-field nanoscopy based on ghost imaging via sparsity constraints, Optica **6**, 1515 (2019).

[33] R. V. Vinu, Z. Y. Chen, R. K. Singh, and J. X. Pu, Ghost diffraction holographic microscopy, Optica **7**, 1697 (2020).

[34] J. Goodman, *Introduction to Fourier Optics* (Macmillan Learning, New York, USA, 2017).

[35] M. Born and E. Wolf, *Principles of Optics: 60th Anniversary Edition* (Cambridge University Press, Cambridge, UK, 2019), 7th ed.

[36] W. Tan, Y. F. Bai, X. W. Huang, T. Jiang, S. Q. Nan, Q. Fu, X. P. F. Zou, and X. Q. Fu, Enhancing critical resolution of a ghost imaging system by using a vortex beam, Opt. Express **30**, 14061 (2022).

[37] W. Tan, X. W. Huang, T. Jiang, S. Q. Nan, Q. Fu, X. P. F. Zou, Y. F. Bai, and X. Q. Fu, Critical resolution in ghost imaging system with pseudo-thermal light, Results Phys. **32**, 105104 (2022).

[38] L. Rayleigh, Investigations in optics, with special reference to the spectroscope, Philos. Mag. **8**, 261 (1879).

[39] R. I. Khakimov, B. M. Henson, D. K. Shin, S. S. Hodgman, R. G. Dall, K. G. Baldwin, and A. G. Truscott, Ghost imaging with atoms, Nature **540**, 100 (2016).

[40] F. Ferri, D. Magatti, L. A. Lugiato, and A. Gatti, Differential Ghost Imaging, Phys. Rev. Lett. **104**, 253603 (2010).

[41] X. R. Yao, W. K. Yu, X. F. Liu, L. Z. Li, M. F. Li, L. A. Wu, and G. J. Zhai, Iterative denoising of ghost imaging, Opt. Express **22**, 24268 (2014).

[42] B. I. Erkmen and J. H. Shapiro, Signal-to-noise ratio of Gaussian-state ghost imaging, Phys. Rev. A **79**, 023833 (2009).

[43] T. S. Tkaczyk, *Field Guide to Microscopy* (Society of Photo Optical, Bellingham, USA, 2010), Vol. 13.

[44] K. Shibuya, H. Araki, and T. Iwata, Photon-counting-based diffraction phase microscopy combined with single-pixel imaging, Jpn. J. Appl. Phys. **57**, 042501 (2018).

[45] S. Liu and H. Hua, Extended depth-of-field microscopic imaging with a variable focus microscope objective, Opt. Express **19**, 353 (2011).